Study of $K^{*-}(890)$ and $K^{*-}(1430)$ production in the reaction $K^-p \to \bar{K}^0\pi^-p$ at 100 and 175 GeV/c

C. Bromberg, J. Dickey, G. Fox, W. Kropac, and S. R. Stampke
California Institute of Technology, Pasadena, California 91125

H. Haggerty and E. Malamud
Fermi National Accelerator Laboratory, Batavia, Illinois 60510

R. Abrams, R. Delzenero, F. Lopez, S. Margulies, D. McLeod, and J. Solomon
University of Illinois at Chicago Circle, Chicago, Illinois 60680

A. Dzierba, F. Fredericksen, R. Heinz, J. Krider, H. Martin, D. V. Petersen, and D. Zieminska
Indiana University, Bloomington, Indiana 47405
(Received 30 January 1984)

The reaction $K^-p \to \bar{K}^0\pi^-p$ has been studied at 100 and 175 GeV/c and the reaction $\pi^-p \to K^0K^-p$ at 50, 100, and 175 GeV/c. Both reactions are dominated by production of resonances, $K^*(890)$, $K^*(1430)$ and $A_2(1320)$, $A_2(2040)$, respectively. Production cross sections, t distributions, and decay-angular distributions are studied. Isoscalar natural-parity exchange is dominant. The energy dependence of the K^* and A_2 resonance production between 10 and 175 GeV/c is well described by a Regge-pole model. Our data on A_2 corrects that in an earlier paper.

I. INTRODUCTION

The multiparticle spectrometer (MPS) was used in the M6 beam line at Fermilab to collect data on various exclusive and semi-inclusive reactions. Several reactions studied in this experiment have been reported on elsewhere.[1-5] In this paper we report on $K^*(890)$ and $K^*(1430)$ production in the reaction

$$K^-p \to \bar{K}^0\pi^-p \tag{1}$$

at 100 and 175 GeV/c. The $K^*(890)$ and $K^*(1430)$ are observed in the $\bar{K}^0\pi^-$ effective-mass distributions relatively free of background. Previous measurements of $K^*(890)$ and $K^*(1430)$ production in reaction (1) have been made at incident laboratory momenta up to 50 GeV/c.[6-14] It has been found that the K^* production is dominated by natural-parity exchange (NPE). We confirm the NPE dominance at incident momenta above 100 GeV/c. We compare the K^* production in reaction (1) with the SU(3)-related A_2 production in the reaction

$$\pi^-p \to K^0K^-p\ , \tag{2}$$

which was also studied in this experiment. We present new results for this reaction which update those in Ref. 2. Our results for both reactions are discussed in the framework of the f-dominated Regge-pole model which has been successfully applied to the K^* and A_2 production in quasi-two-body reactions at lower energies.

The apparatus, event reconstruction, and event weighting are briefly discussed in Sec. II. The resonance-production cross sections and the $p_{\rm LAB}$ dependence are presented in Sec. III. Section III also includes a discussion of t distributions and of the decay-angular distributions of the observed resonances. In Sec. IV we discuss our data on reaction (2). In Sec. V we describe the f-dominated Pomeron model and its implications for reactions (1) and (2) with our data. Section VI is a summary of our conclusions.

II. APPARATUS AND ANALYSIS

The Fermilab multiparticle spectrometer (MPS) shown in Figs. 1 and 2 is located in the M6 beam line. This beam line contained four gas Čerenkov counters which allowed separation of pions, kaons, and antiprotons. Details of the MPS hardware are given in Refs. 4 and 5. Only those aspects of the MPS relevant to this reaction are discussed here.

The trigger for this reaction is the same as for the reaction $\pi^-p \to K^0K^-p$ discussed in Ref. 2. The only difference is that the beam particle is required to be a K^-. Figure 2 shows the trigger requirements, which demanded that the final state contain a single charged particle in the forward direction in addition to a recoil proton and a neutral "vee" decaying into two charged particles within a specific decay volume. In Fig. 2, $V0$ through $V3$ are shower counters. Ax through Dy and β are proportional wire chambers (PWC's). $V1$ and β are cylindrical in geometry and are concentric with the foot-long, 1-in.-diam cylindrical liquid hydrogen target. The presence of a signal in any of the shower counters vetoed events with π^0 mesons in the nonforward direction. Hit multiplicities detected in the PWC's required the event topology described above. A change in multiplicity from 1 in the A PWC's to 3 in the BCD PWC's defined the K^0 decay volume as shown in Fig. 2.

The momenta and directions of the forward-going charged particles were determined by using the tracking system consisting of PWC's and magnetostrictive wire

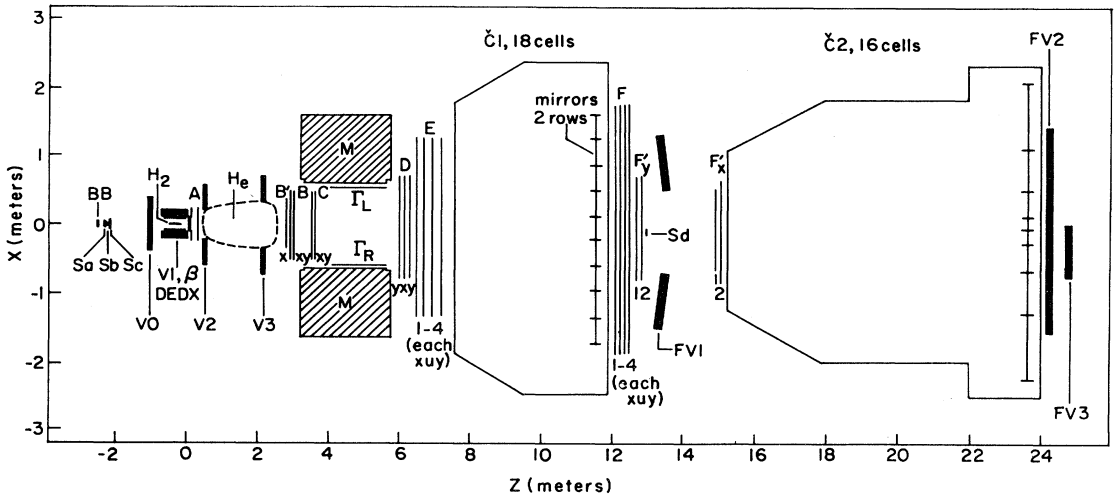

FIG. 1. Multiparticle spectrometer, plan view. *Sa*, *Sb*, *Sc*, *DEDX*, and *Sd* are scintillation counters. *V*0, *V*1, *V*2, and *V*3 are veto shower counters. *BB*, *A*, *B'*, *B*, *C*, *D*, *F'*, β and Γ are proportional wire chambers. *E* and *F* are sets of wire spark chambers. *C*1 and *C*2 are segmented gas Čerenkov counters. *FV*1, *FV*2, and *FV*3 are forward γ detectors.

spark chambers and a large-aperture superconducting magnet. The magnet was operated at a central field strength of 17.8 kG and had an effective length of 1.4 m, imparting a transverse momentum of 0.75 GeV/c.

The track-finding and event-reconstruction program used on these data, *E*110 *TEARS*, is described in Refs. 4 and 5. The reconstruction requirements peculiar to this trigger are discussed in Ref. 2. In order to reduce background from events with missing neutrals we applied restrictions on the total visible energy $E_{\rm TOT}$: $96 < E_{\rm TOT} < 104$ GeV and $161 < E_{\rm TOT} < 184$ GeV for the 100-GeV/c and 175-GeV/c data, respectively, as shown in Fig. 3. The total number of selected events is 348 and 173 at the two incident momenta, respectively.

III. REACTION $K^-p \to K^0\pi^-p$

A. $\overline{K}{}^0\pi$ effective mass

The $\overline{K}{}^0\pi$ effective mass is shown in Fig. 4(a) for the 100-GeV/c data in Fig. 4(b) for the 175-GeV/c data. The mass spectra at both incident momenta are consistent with the $K^*(890)$ and $K^*(1430)$ production with no nonresonant background. There is no clear evidence for production of the $K^*(1780)$ decaying into $\overline{K}{}^0\pi^-$.

B. $K^{*-}(890)$ and $K^{*-}(1430)$ production cross sections

The major uncertainty in estimating the K^* resonance production in reaction (1) in our experiment is a back-

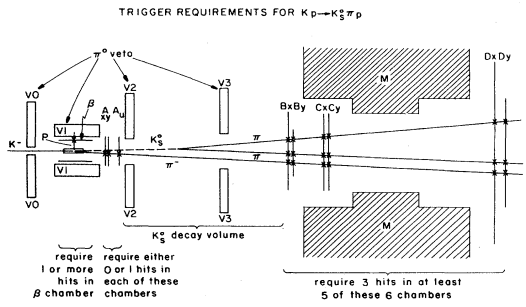

FIG. 2. Multiparticle spectrometer front end, side view, and diagram of trigger requirements.

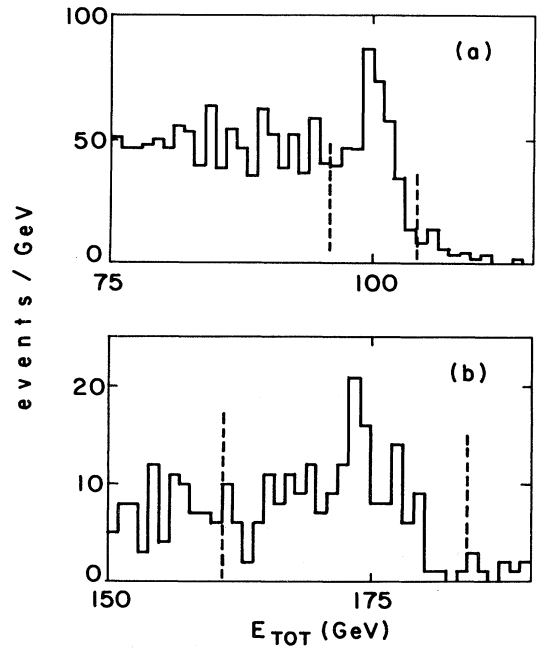

FIG. 3. Distributions of the total energy of the $\overline{K}{}^0\pi^-$ system in laboratory frame, $E_{\rm TOT}$, for (a) $P_{\rm LAB}=100$ GeV/c and (b) $P_{\rm LAB}=175$ GeV/c.

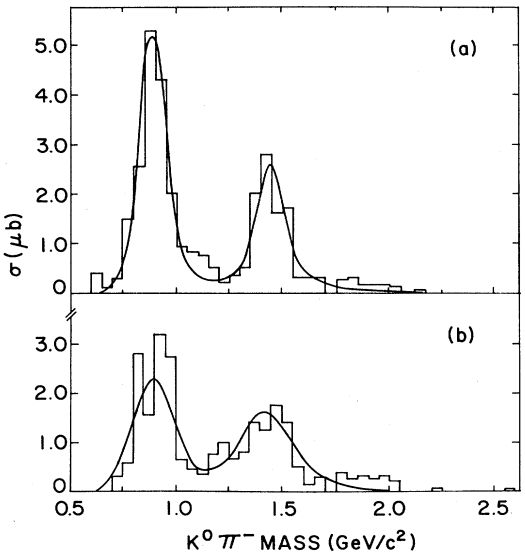

FIG. 4. $\bar{K}^0\pi^-$ effective-mass distribution for (a) $P_{LAB}=100$ GeV/c and (b) $P_{LAB}=175$ GeV/c. The curves represent Breit-Wigner functions with parameters taken from Ref. 6, corrected for experimental mass resolution.

ground from events with undetected neutral particles, which is not removed entirely by imposing restrictions on the total visible energy. In Fig. 5 we show the E_{TOT} distributions for the 100-GeV/c and 175-GeV/c data in the $(K\pi)$ mass region of the $K^*(890)$ $(0.84<M<0.94$ GeV/c^2, and $0.76<M<1.04$ GeV/c^2, respectively) and the $K^*(1430)$ $(1.28<M<1.60$ GeV/c^2). We see that in the case of the $K^*(1430)$ the distributions are peaked around the values of the incident energy, with no significant background. On the other hand, the E_{TOT} distributions in the $K^*(890)$ range indicate a large background. We estimate the cross sections for the $K^*(890)$ and $K^*(1430)$ production in reaction (1) by performing a least-squares fit to the data presented in Fig. 5. We assume a background decreasing linearly with energy and extending to $E_{TOT}=100$ GeV and $E_{TOT}=175$ GeV for the two data samples, respectively. We further allow for a finite-

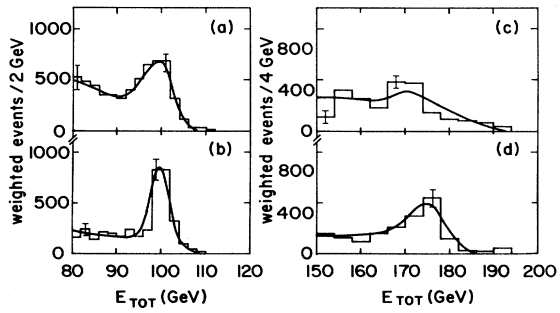

FIG. 5. E_{TOT} distributions for (a) $K^*(890)$ band, at $P_{LAB}=100$ GeV/c, (b) $K^*(1430)$ band, at $P_{LAB}=175$ GeV/c, (c) $K^*(890)$ band, at $P_{LAB}=100$ GeV/c, and (d) $K^*(1430)$ band, at $P_{LAB}=175$ GeV/c.

TABLE I. Cross sections for reaction $K^-p\to\bar{K}^0\pi^-p$. Units are μb. The first three rows give cross sections within the $K^*(890)$ and $K^*(1430)$ mass cuts. The fourth and fifth rows give the products of production cross sections and branching ratios for both K^* resonances. The last two line rows give the corresponding total production cross sections. The errors are statistical. The systematic errors are 30 and 50% at 100 and 175 GeV/c, respectively.

	100 GeV/c	175 GeV/c
$\sigma(0.84<M<0.94$ GeV/$c^2)$	10.3±1.5	
$\sigma(0.76<M<1.04$ GeV/$c^2)$		5.4±1.0
$\sigma(1.28<M<1.60$ GeV/$c^2)$	9.9±1.0	5.4±0.6
$\sigma(K^*(890))B(K^*\to\bar{K}^0\pi^-)$	23.9±2.5	6.0±1.2
$\sigma(K^*(1430))B(K^*\to\bar{K}^0\pi^-)$	12.7±1.3	8.4±0.8
$\sigma(K^-p\to K^{*-}(890)p)$	35.9±3.8	9.0±1.8
$\sigma(K^-p\to K^{*-}(1430)p)$	42.5±4.0	28.1±2.7

energy resolution by smearing the assumed distribution according to the Gaussian function. To correct for the tails of the K^* mass distributions we ascribe all events with $M(K\pi)$ less (greater) than 1.20 GeV/c^2 to $K^*(890)$ ($K^*(1430)$). The resulting values of the production cross sections are given in Table I along with statistical error bars. There is an additional systematic uncertainty of 30 and 50% in the case of $K^*(890)$ at 100 and 175 GeV/c, respectively, due to estimating the background. For $K^*(1430)$ production the estimated systematic error is 10%. In calculating the total production cross sections we assumed the value of the branching ratio $B(K^*(1430)\to K\pi)=0.448$ (Ref. 15). Our results are consistent with the measurements of the cross sections at lower incident momenta, as seen in Fig. 6.

C. Momentum-transfer distributions

We have measured the differential cross sections $d\sigma/dt$ for $K^*(1430)$ and $K^*(890)$ production. The $d\sigma/dt$ distributions for $K^*(890)$ events at 100 and 175 GeV/c are

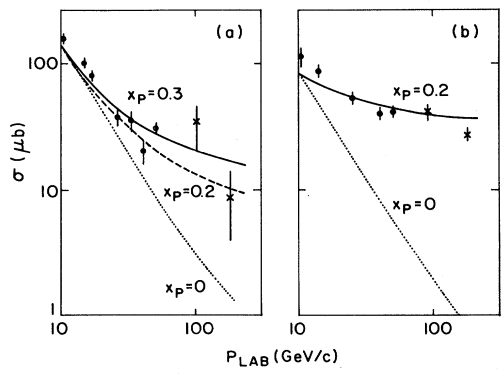

FIG. 6. Production cross section for (a) $K^*(890)$ and (b) $K^*(1430)$ resonance as a function of incident momentum. Systematic errors are included in error bars. The curves are calculated according to the model of Ref. 17. The crosses represent the data points from this experiment.

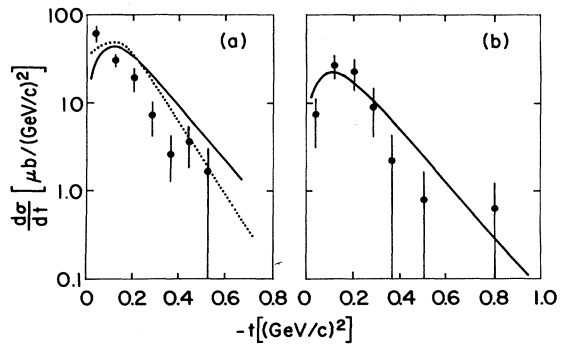

FIG. 7. The differential cross sections in the $K^*(890)$ region for (a) $P_{LAB}=100$ GeV/c, (b) $P_{LAB}=175$ GeV/c, $E_{TOT}>170$ GeV. The solid curves in (a) and (b) are calculated from the model of Ref. 17 with $x_P=0.3$. The dotted curve is calculated with $x_P=0$.

shown in Fig. 7. The $M(K\pi)$ mass requirements are the same as in Sec. III B. For the $P_{LAB}=175$-GeV/c data the more severe selection, $170<E_{TOT}<184$, was made to reduce background. The $d\sigma/dt$ distributions for $K^*(1430)$ events are shown in Figs. 8(a) and (b).

D. Decay-angular distributions

Below we discuss the angular distributions of the π^- mesons from the K^* decay in the t-channel helicity (Gottfried-Jackson) frame. In general, the probability for a decay of a spin-J particle into spinless particles, in the direction (θ,ϕ) is given by

$$I(\theta,\phi)=N\sum\cos[(m-m')\phi]\,|\,Y_J^m(\theta)\,||\,Y_J^{m'}(\theta)\,|\,\rho_{mm'}\,, \tag{3}$$

where ρ is the K^* spin-space density matrix. The dominant NPE contribution populates K^* states with helicities $m=0$. Furthermore, if we neglect production of $K^*(1430)$ states with $m>1$, and apply the restrictions on the density matrix, $\mathrm{Tr}\rho=1$, $\mathrm{Tr}\rho^2=1$, the ρ matrix for both K^* resonances reduces to

$$\rho=\begin{bmatrix} \frac{1}{2} & 0 & \frac{1}{2} \\ 0 & 0 & 0 \\ \frac{1}{2} & 0 & \frac{1}{2} \end{bmatrix}, \tag{4}$$

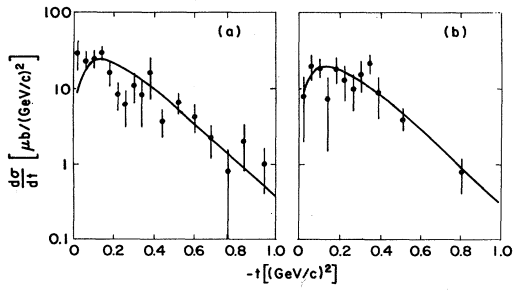

FIG. 8. The differential cross sections in the $K^*(1430)$ region at (a) $P_{LAB}=100$ GeV/c and (b) $P_{LAB}=175$ GeV/c. The curve is calculated from the model of Ref. 17, with $x_P=0.2$.

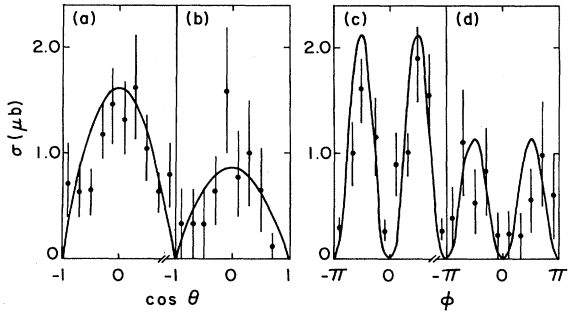

FIG. 9. Decay-angular distributions in the $K^*(890)$ region. (a) $\cos\theta$ at $P_{LAB}=100$ GeV/c, (b) $\cos\theta$ at $P_{LAB}=175$ GeV/c, (c) Φ at $P_{LAB}=100$ GeV/c, (d) Φ at $P_{LAB}=175$ GeV/c. The curves are given by Eqs. (5a) and (5b).

and we obtain

$$I(\theta,\phi)=2\sin^2\phi\,|\,Y_J^1(\theta)\,|^2\,. \tag{5}$$

The projected distributions $I(\theta)$ and $I(\phi)$ for $J=1$ [$K^*(890)$] and $J=2$ [$K^*(1430)$] are

$$J=1:\begin{cases} I(\theta)\propto\sin^2\theta, & \text{(6a)} \\ I(\phi)\propto\sin^2\phi, & \text{(6b)} \end{cases}$$

and

$$J=2:\begin{cases} I(\theta)\propto\sin^2\theta\cos^2\theta, & \text{(7a)} \\ I(\phi)\propto\sin^2\phi. & \text{(7b)} \end{cases}$$

Results for the projected distributions for $K^*(890)$ and $K^*(1430)$ production at 100 and 175 GeV/c are shown in Figs. 9 and 10, respectively. Also shown are curves given by Eqs. (6) and (7). Our results confirm the dominance of the helicity $m=\pm1$ production for both $K^*(890)$ and $K^*(1430)$ resonances, and thus, confirm the dominant role of NPE for reaction (1).

IV. REACTION $\pi^-p\to K^0K^-p$

Reaction (2) has been studied in this experiment at beam momenta 50, 100, and 175 GeV/c. The K^0K^-

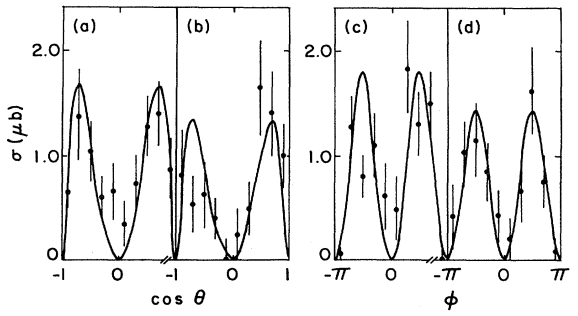

FIG. 10. Decay-angular distributions in the $K^*(1430)$ region. (a) $\cos\theta$ at $P_{LAB}=100$ GeV/c, (b) $\cos\theta$ at $P_{LAB}=175$ GeV/c, (c) ϕ at $P_{LAB}=100$ GeV/c, (d) ϕ at $P_{LAB}=175$ GeV/c. The curves are given by Eqs. (7a) and (7b).

TABLE II. Cross sections for reaction $\pi^- p \to A_2 p$. Units are μb. The first two rows give cross-section times branching ratio for $A_2(1320)$ and $A_2(2040)$. The third row gives the total cross section for $\pi^- p \to A_2(1320)p$.

	50 GeV/c	100 GeV/c	175 GeV/c
$\sigma(\pi^- p \to A_2(1320)p)B(A_2 \to K^0 K^-)$	2.56±0.25	1.41±0.04	1.24±0.05
$\sigma(\pi^- p \to A_2(2040)p)B(A_2 \pm K^0 K^-)$	0.46±0.04	0.41±0.04	0.51±0.05
$\sigma(\pi^- p \to A_2(1320))$	53±4	29±1	26±1

mass spectrum extends from threshold to 3.2 GeV/c^2. Some results have been reported in Ref. 2, with an emphasis on the $A_2(1320)$ region. In particular, the total cross section for reaction (2) was measured and the cross section for the $A_2(1320)$ production was estimated assuming a D-wave Breit-Wigner resonance with parameters taken from the Particle Data Group tables[15] and a nonresonant background. The effect of finite-energy resolution was neglected leading to underestimated cross sections for A_2 production. The present study of the K^0K^- spectrum and of the angular distributions in the whole mass range indicates that this reaction is strongly dominated by two NPE amplitudes D_+ and G_+, which are identified with the $A_2(1320)$ resonance and the spin-4 resonance $A_2(2040)$. We estimate the production cross sections for both resonances by assigning all events at $M(K^0K^-) < 1.9$ GeV/c^2 to $A_2(1320)$ and the rest to $A_2(2040)$. The systematic error involved in this estimate is less than 10% for $A_2(1320)$ and less than 50% for $A_2(2040)$. The results are given in Table II and in Fig. 11, where the cross sections are plotted as functions of beam momentum.

To study the momentum-transfer distributions and decay-angular distributions, we select three K^0K^- mass bands: the $A_2(1320)$ range, $1.22 < M(K^0K^-) < 1.42$ GeV/c^2, an intermediate region, $1.50 < M(K^0K^-) < 1.80$ GeV/c^2 and the $A_2(2040)$ range, $1.80 < M(K^-K^0) < 2.40$ GeV/c^2. The corresponding t distributions are shown in Fig. 12. The last two distributions are normalized to the first one. We find the momentum-transfer distributions in the three regions to be the same within statistical uncertainty.

The angular distributions in the t-channel helicity frame for the 100-GeV/c data are shown in Fig. 13. For the first two K^0K^- mass ranges the curves are appropriate for the D_+ wave, as given in Eqs. (7a) and (7b). The data in the third mass range show the presence of the G_+ wave ($J=4$) and the high-mass tail of the $A_2(1320)$ resonance. The curve was calculated assuming $|D_+| = |G_+|$ and the relative phase, $\cos\Phi_{D_+G_+} = 0.2$. It accounts well for our data and is compatible with results of Ref. 16.

V. COMPARISON WITH REGGE MODEL

In the Regge-pole theory the production of meson resonances in reactions (1) and (2) proceed through the exchange of the natural-parity Regge trajectories Pomeron P, f, and ω in (1) and P and f in (2). In the case of exact SU(3) symmetry the Pomeron is a pure SU(3) singlet, and thus gives equal contributions to the production of $K^*(1430)$ and $A_2(1320)$ which are members of the same nonet. Also, its contribution to the $K^*(890)$ production vanishes by virtue of generalized C-parity conservation.

In the f-dominated Pomeron model,[17] the Pomeron is

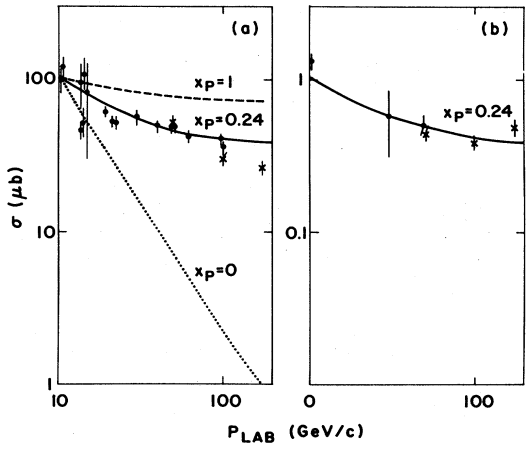

FIG. 11. Production cross section for (a) $A_2(1320)$ and (b) $A_2(2040)$ resonance (2) as functions of incident momentum. The curves are calculated from the model of Ref. 17 with $x_P = 0.24$. The crosses represent the data points from this experiment.

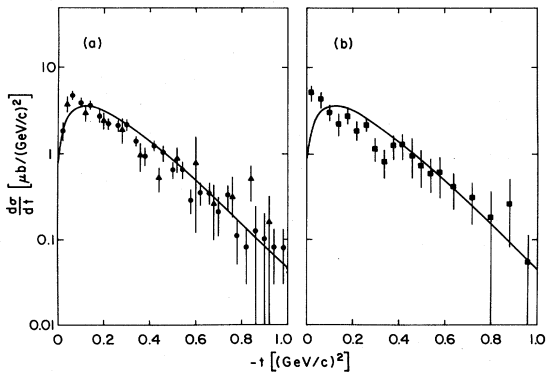

FIG. 12. The differential cross sections for reaction (2) at 100 GeV/c, for (a) $1.22 < M(K^0K^-) < 1.42$ GeV/c^2 (circles) and $1.80 < M(K^0K^-) < 2.40$ GeV/c^2 (triangles), (b) $1.50 < M(K^0K^-) < 1.80$ GeV/c^2. The last two distributions were multiplied by the factors 3.2 and 2.5, respectively, to normalize them to the area of the first distribution.

assumed to couple to external particles via the f and f' mesons. The model allows for some SU(3) breaking due to the difference between the f and f' masses. The amplitudes for the K^* production in reaction (1) can be written as[17]

$$T(K^*)=FP+f+\omega\ , \tag{8}$$

$$P(t)=-\frac{\sqrt{-t}}{2m_p}\beta_{pp}^{f}\beta_{f}^{KK^*}(0.71x_p)\exp(At)\exp[-\tfrac{1}{2}i\pi\alpha_p(t)](\alpha's)^{\alpha_P(t)}\ , \tag{9a}$$

$$f(t)=-\frac{\sqrt{-t}}{2m_p}\beta_{pp}^{f}\beta_{f}^{KK^*}\tfrac{1}{2}\{1+\exp[-i\pi\alpha_f(t)]\}\Gamma(1-\alpha_f(t))(\alpha's)^{\alpha_f(t)}\ , \tag{9b}$$

$$\omega(t)=\frac{\sqrt{-t}}{2m_p}\beta_{pp}^{\omega}\beta_{\omega}^{KK^*}\tfrac{1}{2}\{1-\exp[-i\pi\alpha_\omega(t)]\}\Gamma(1-\alpha_\omega(t))(\alpha's)^{\alpha_\omega(t)}\ . \tag{9c}$$

The factor F in Eq. (8) is given by

$$F(t)=1-r(t)\ \text{ for } K^*(890)\ , \tag{10a}$$

$$F(t)=1+r(t)\ \text{ for } K^*(1430)\ . \tag{10b}$$

The function

$$r(t)=\frac{\alpha_P(t)-\alpha_f(t)}{\alpha_P(t)-\alpha_{f'}(t)} \tag{11}$$

represents the SU(3) mass breaking. To compare our data with the predictions of the model we use the following trajectories: $\alpha_P=1.04+0.2t$, $\alpha_f=\alpha_\omega=0.4+t$. Coupling constants and the slope parameter A in the Pomeron amplitude are taken as in Ref. 14.

The behavior of the cross sections as functions of the incident momentum is sensitive to the relative P/f coupling strength x_P. For the $K^*(890)$ and $K^*(1430)$ production the values $x_P=0.3$, and $x_P=0.2$, respectively, gave the best fit to the high-statistics data[14] at incident momenta $P_{\rm LAB}=10$, 30, and 50 GeV/c. As seen in Fig. 6, our results are in good agreement with previously determined values of x_P. For $A_2(1320)$ $x_P=0.24\pm0.02$ was obtained in Ref. 16. The corresponding curve is shown in Fig. 11. Our results at 100 and 175 GeV/c lie below this curve, suggesting a slightly lower value of x_P. Our estimated cross sections for $A_2(2040)$ production are in agreement with earlier data.

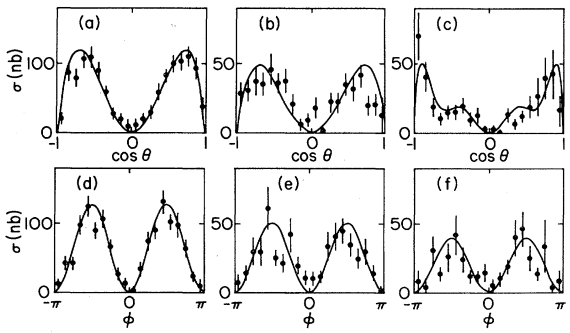

FIG. 13. Decay-angular distributions for reaction (2). (a) $\cos\theta$, $1.22<M(K^0K^-)<1.42$ GeV/c^2, (b) $\cos\theta$, $1.50<M(K^0K^-)<1.80$ GeV/c^2, (c) $\cos\theta$, $1.80<M(K^0K^-)<2.40$ GeV/c^2, (d) Φ, $1.22<M(K^0K^-)<1.42$ GeV/c^2, (e) Φ, $1.50<M(K^0K^-)<1.80$ GeV/c^2, (f) Φ, $1.80<M(K^0K^-)<2.40$ GeV/c^2.

It is often assumed that the Pomeron is an SU(3) singlet, and thus its contribution to $K^*(890)$ production in reaction (1) vanishes. It corresponds to the $\alpha_f=\alpha_{f'}$ limit in Eq. (11) for which $r(t)=1$. The amplitude for $K^*(890)$ production [Eq. (8)] is then limited to the f and ω terms. It coincides with the choice $x_P=0$, represented by a dotted curve in Fig. 6. Our results favor the scheme allowing for nonzero Pomeron-exchange contribution to reaction $K^-p\to K^{*-}(890)p$. We thus see clear evidence for SU(3) breaking for the Pomeron, and the f-dominated Pomeron is a particular model for this which agrees with our data.

The data on the differential cross sections $d\sigma/dt$ provide an independent test of the model. Generally, the x_P values between 1 and 0.2 give very similar predictions due to the strong domination of the Pomeron term. The curves in Figs. 7, 8, and 12 are drawn for the x_P values as determined in Refs. 14 and 16. The $K^*(1430)$ data (Fig. 7) and the A_2 data (Fig. 23) are in very good agreement with the predicted distributions. The $x_P=0$ assignment is incompatible with the data, leading to distributions which are too steep. The $d\sigma/dt$ distributions for $K^*(890)$ (Fig. 8) are considerably steeper than predicted by the model, and are in a better agreement with the dotted curve obtained for the f and ω contributions alone. However, this discrepancy may be partially due to the presence of considerable background in this case.

VI. SUMMARY

We have studied the reaction $K^-p\to\bar{K}^0\pi^-p$ at 100 and 175 GeV/c and the reaction $\pi^-p\to K^0K^-p$ at 50, 100, and 175 GeV/c. We find the $(\bar{K}^0\pi^-)$ invariant mass distributions to be completely dominated by the $K^*(890)$ and $K^*(1430)$ resonances and (K^0K^-) mass distributions dominated by $A_2(1320)$ and $A_2(2040)$ resonances. The K^* and A_2 production cross sections are consistent with results at lower energies and agree well with the f-dominated Pomeron-exchange model. The differential cross sections $d\sigma/dt$ are also consistent with the model except for the case of $K^*(890)$, where the f and ω exchange alone account better for the data. The decay-angular distributions confirm the dominant role of the natural-parity exchange.

[1]C. Bromberg *et al.*, Phys. Rev. D 22, 1513 (1980).
[2]C. Bromberg *et al.*, Phys. Rev. D 27, 1 (1983).
[3]C. Bromberg *et al.*, Phys. Rev. D 29, 588 (1984).
[4]F. Fredericksen, Ph.D. thesis, Indiana University, 1982.
[5]S. Stampke, Ph.D. thesis, California Insitute of Technology, 1982.
[6]CERN/HERA Data Compilation, Report No. CERN-HERA 79-02, 1979.
[7]R. Baldi *et al.*, Phys. Lett. 70B, 377 (1977).
[8]R. Baldi *et al.*, Nucl. Phys. B134, 365 (1978).
[9]A. D. Martin, *et al.*, Nucl. Phys. B134, 392 (1978).
[10]A. C. Irving *et al.*, Nucl. Phys. B149, 101 (1979).
[11]A. Givernaud *et al.*, Nucl. Phys. B153, 280 (1979).
[12]W. E. Cleland *et al.*, Phys. Lett. 97B, 465 (1980).
[13]A. Delfosse *et al.*, Nucl. Phys. B183, 349 (1981).
[14]W. E. Cleland, *et al.*, Nucl. Phys. B208, 189 (1982).
[15]Particle Data Group, Phys. Lett. 111B, 1 (1982).
[16]W. E. Cleland, *et al.*, Nucl. Phys. B208, 228 (1982).
[17]R. Carlitz *et al.*, Phys. Rev. D 4, 3439 (1971); A. C. Irving, Nucl. Phys. B121, 176 (1977).